Multicomponent fluid model for two-temperature plasmas derived from kinetic theory : application to magnetic reconnection

IOP Conf. Series: Journal of Physics: Conf. Series **1125** (2018) 012021 doi:10.1088/1742-6596/1125/1/012021

Multicomponent fluid model for two-temperature plasmas derived from kinetic theory : application to magnetic reconnection

Q. Wargnier[1], A. Alvarez Laguna[2], P. Kestener[3], B. Graille[4], N. N. Mansour[5], T. Magin[6], and M. Massot[1]

[1] Centre de Mathématiques Appliquées, Ecole polytechnique, CNRS, Palaiseau, France
[2] Laboratoire de Physique des Plasmas, Ecole Polytechnique, CNRS, Palaiseau, France
[3] Maison de la Simulation, CEA, CNRS, Saclay, France
[4]Laboratoire de Mathématiques d'Orsay, Univ. Paris-Sud, CNRS, Université Paris-Saclay, 91405 Orsay, France
[5] NASA Ames Research Center, Moffett Field, California, USA
[6]Aeronautics & Aerospace Dept., von Karman Institute for Fluid Dynamics, Rhode-St.-Genèse, Belgium

E-mail: quentin.wargnier@polytechnique.edu

Abstract. This contribution deals with the fluid modeling of multicomponent magnetized plasmas in thermo-chemical non-equilibrium from the partially- to fully-ionized collisional regimes, aiming at the predictive simulation of magnetic reconnection in Sun chromosphere conditions. Such fluid models are required for large-scale simulations by relying on high performance computing. The fluid model is derived from a kinetic theory approach, yielding a rigorous description of the dissipative and non-equilibrium effects and a well-identified mathematical structure. We start from a general system of equations that is obtained by means of a multiscale Chapman-Enskog method, based on a non-dimensional analysis accounting for the mass disparity between the electrons and heavy particles, including the influence of the electromagnetic field and transport properties. The latter are computed by using a spectral Galerkin method based on a converged Laguerre-Sonine polynomial approximation. Then, in the limit of small Debye length with respect to the characteristic scale in the Sun chromosphere, we derive a two-temperature single-momentum multicomponent diffusion model coupled to Maxwell's equations, which is able to describe fully- and partially-ionized plasmas, beyond the multi-fluid model of Braginskii, valid for the whole range of the Sun chromosphere conditions. The second contribution is the development and verification of an accurate and robust numerical strategy that is based on CanoP, a massively parallel code with adaptive mesh refinement capability, which is able to cope with the full spectrum of scales of the magnetic reconnection process, without additional constraint on the time steps compared to single-fluid Magnetohydrodynamics (MHD) models. The final contribution is a study of the physics of magnetic reconnection in collaboration with the heliophysics team of NASA Ames Research Center. We show that the model and methods allow us to retrieve the results of usual single-fluid MHD models in the highly collisional case at equilibrium, while achieving a more detailed physics description relevant to such applications in the weakly collisional case, where non-equilibrium effects become important.

1. Introduction

Magnetic reconnection is a process where the topology of the magnetic field lines is modified due to dissipative effects. Lines of different polarity are broken and rejoined in a small diffusion region, leading to conversion of the magnetic energy into plasma kinetic and thermal energy. This phenomenon is

not captured correctly by ideal models. Leake *et al.* [1] have simulated the magnetic reconnection phenomenon for a weakly ionized reacting plasma in Sun chromosphere conditions by means of a self-consistent multi-fluid model. In this context, when the characteristic scale of the current sheet width is comparable to the collisional mean-free-path, a decoupling of ions from neutrals and enhanced recombination in the reconnection region are observed. This decoupling cannot be captured by conventional single-fluid MHD models, whereas multi-fluid model lead to extreme stiffness, which is hard to resolve numerically [2, 3].

However, Graille *et al.* [4] have developed a two-temperature single-momentum multicomponent diffusion model as an alternative to multi-fluid models [5, 6, 7, 2, 3, 8] to describe fully- and partially-ionized plasmas, beyond the multi-fluid model of Braginskii (valid only for fully-ionized plasma) and with a solid mathematical structure [4]. The model is obtained rigorously from kinetic theory using a multiscale Chapman-Enskog expansion combining the usual Knudsen number and the mass ratio between electrons and heavy species. This leads to a system of equations that is less stiff as the electron inertia is neglected.

In this paper, we first couple this model to Maxwell's equations and derive the asymptotic limit of small Debye length, which is reasonable considering the size of the Debye length with respect to the characteristic scales representative of the Sun atmosphere. The resulting model is derived and allows us to describe fully and partially ionized plasmas; it is valid for the whole range of the Sun chromosphere conditions and should be an interesting alternative to study magnetic reconnection. We check that we recover the usual single-fluid MHD model under temperature equilibrium and isotropic transport properties. Then, we propose an accurate and robust numerical strategy relying on a finite volume approach and based on the `CanoP` code [9, 10]. `CanoP` is a massively parallel code with adaptive mesh refinement capability managed by the `p4est` library [11], which is able to cope with the full spectrum of scales of the magnetic reconnection process, without additional constraint on the time steps as compared to multi-fluid MHD models. We have coupled the `CanoP` code to the `MUTATION++` library [12] and it gives the possibility to compute thermodynamic properties, multicomponent transport properties with high accuracy, finite rate chemistry in thermal non-equilibrium. The numerical strategy is verified through several standard test-cases used as benchmarks in the community and we refer to [13, 14] for further verifications/validations concerning the `MUTATION++` library and the `CanoP` code for magnetized plasma out of thermal equilibrium and parallel capabilities. Finally, we propose a comparison between the two-temperature single-momentum multicomponent diffusion model and the single-fluid MHD model for a magnetic reconnection configuration under Sun chromosphere condition in several collisional regimes. The model and numerical strategy are assessed and we discuss the potential of our approach.

2. Two-temperature single-momentum multicomponent diffusion model

In this section, we briefly describe the multicomponent plasma model that is derived from kinetic theory by Graille *et al.* [4]. The model is suitable for both partially- and fully-ionized multicomponent plasmas. Moreover, it accounts for the thermal non-equilibrium between the heavy particles (ions and neutrals) and the electrons as well as for the anisotropy in the transport properties that is introduced by the magnetic field. In the present work, we propose to apply the mentioned model to the simulation of the Sun chromosphere as a sound alternative to multi-fluid models.

2.1. Multi-scale analysis of the Boltzmann equations

Multi-fluid models can be obtained by taking moments of Boltzmann's equation (see e.g., [15, 16, 17, 7]) while the present model, prior to taking the moments, examines the different scales of the kinetic equation for electrons and heavy particles through a dimensional analysis. The separation of scales in the Boltzmann equation are caused by the mass disparity between the electrons and the heavy species as well as by the level of magnetization of the different charged species. In the following, we present the

normalized Boltzmann's equations for electrons and heavy particles in order to illustrate the derivation of the model. For more details, we may refer the reader to the work of Graille *et al.* [4].

For the normalization of Boltzmann's equations, we introduce three parameters: ε the square root of the electron-to-heavy-particle mass ratio, $\mathcal{K}_n$ the Knudsen number, and $M_\mathfrak{h}$ the pseudo-Mach number of the heavy particles as

$$\varepsilon = \sqrt{\frac{m_\mathfrak{e}}{m_\mathfrak{h}}}, \quad \mathcal{K}_n = \frac{l}{\mathcal{L}} \sim \varepsilon, \quad \text{and} \quad M_\mathfrak{h} = \frac{v}{V_\mathfrak{h}} \sim 1. \tag{1}$$

Here, $m_\mathfrak{e}$ stands for the mass of electron, $m_\mathfrak{h}$ for a characteristic mass of heavy particle, l for the mean free path, $\mathcal{L}$ for a macroscopic length scale, v for the reference hydrodynamic velocity and $V_\mathfrak{h}$ for the heavy-particle thermal speed. Note that the model assumes the Knudsen number to be small and of order ε. Additionally, the pseudo-Mach number of the heavy particles is assumed to be of order one.

Similarly, the magnetization of the charged species is quantified by the Hall parameter, which is defined as

$$\beta_\mathfrak{e} = \frac{qB}{m_\mathfrak{e}} t_\mathfrak{e} = \varepsilon^{1-b}, \quad \beta_\mathfrak{h} = \frac{qB}{m_\mathfrak{h}} t_\mathfrak{h} = \varepsilon \beta_\mathfrak{e}, \tag{2}$$

where $qB/m_\mathfrak{e}$ and $qB/m_\mathfrak{h}$ are the Larmor frequencies of electrons and heavy particles, respectively, and $t_\mathfrak{e}$ and $t_\mathfrak{h}$ the typical time between collisions for electrons and ions. The Hall parameter is assumed to be proportional to a power of ε by means of an integer b that characterizes its intensity: $b < 0$ for unmagnetized plasmas, $b = 0$, for weakly magnetized plasmas, and $b = 1$ for strongly magnetized plasmas [4].

These non-dimensional quantities are then used to write the normalized Boltmann's equations. First, the kinetic equation of electrons reads

$$\begin{aligned} \partial_t \boldsymbol{f}_\mathfrak{e} + \frac{1}{\varepsilon M_\mathfrak{h}} (\boldsymbol{C}_\mathfrak{e} + \varepsilon M_\mathfrak{h} \boldsymbol{v}_\mathfrak{h}) \cdot \boldsymbol{\partial_x} \boldsymbol{f}_\mathfrak{e} + \varepsilon^{-(1+b)} \mathfrak{q}_\mathfrak{e} \Big[(\boldsymbol{C}_\mathfrak{e} + \varepsilon M_\mathfrak{h} \boldsymbol{v}_\mathfrak{h}) \wedge \boldsymbol{B} \Big] \cdot \partial_{\boldsymbol{C}_\mathfrak{e}} \boldsymbol{f}_\mathfrak{e} \\ + \left(\frac{1}{\varepsilon M_\mathfrak{h}} \mathfrak{q}_\mathfrak{e} \boldsymbol{E} - \varepsilon M_\mathfrak{h} \frac{D\boldsymbol{v}_\mathfrak{h}}{Dt} \right) \cdot \partial_{\boldsymbol{C}_\mathfrak{e}} \boldsymbol{f}_\mathfrak{e} - (\partial_{\boldsymbol{C}_\mathfrak{e}} \boldsymbol{f}_\mathfrak{e} \otimes \boldsymbol{C}_\mathfrak{e}) \colon \boldsymbol{\partial_x} \boldsymbol{v}_\mathfrak{h} = \frac{1}{\varepsilon^2} \mathcal{J}_\mathfrak{e}. \end{aligned} \tag{3}$$

Second, the kinetic equation for the heavy species is given by

$$\begin{aligned} \partial_t \boldsymbol{f}_i + \frac{1}{M_\mathfrak{h}} (\boldsymbol{C}_i + M_\mathfrak{h} \boldsymbol{v}_\mathfrak{h}) \cdot \boldsymbol{\partial_x} \boldsymbol{f}_i + \varepsilon^{1-b} \mathfrak{q}_i \Big[(\boldsymbol{C}_i + M_\mathfrak{h} \boldsymbol{v}_\mathfrak{h}) \wedge \boldsymbol{B} \Big] \cdot \partial_{\boldsymbol{C}_i} \boldsymbol{f}_i \\ + \left(\frac{1}{M_\mathfrak{h}} \frac{\mathfrak{q}_i}{m_i} \boldsymbol{E} - M_\mathfrak{h} \frac{D\boldsymbol{v}_\mathfrak{h}}{Dt} \right) \cdot \partial_{\boldsymbol{C}_i} \boldsymbol{f}_i - (\partial_{\boldsymbol{C}_i} \boldsymbol{f}_i \otimes \boldsymbol{C}_i) \colon \boldsymbol{\partial_x} \boldsymbol{v}_\mathfrak{h} = \frac{1}{\varepsilon} \mathcal{J}_i, \quad i \in \mathrm{H}. \end{aligned} \tag{4}$$

Here, $\boldsymbol{f}_\mathfrak{e}$ and $\boldsymbol{f}_i$, $i \in \mathrm{H}$, are respectively the distribution function of the electrons and heavy particles with H the set of heavy particles present in the plasma. The peculiar velocities for heavy species and electrons are $\boldsymbol{C}_i = \boldsymbol{c_i} - \boldsymbol{v}_\mathfrak{h}$ and $\boldsymbol{C}_\mathfrak{e} = \boldsymbol{c_e} - \boldsymbol{v}_\mathfrak{h}$. The collision operators $\mathcal{J}_\mathfrak{e}$ and $\mathcal{J}_i$ are defined as

$$\mathcal{J}_\mathfrak{e} = \mathcal{J}_{\mathfrak{e}\mathfrak{e}}(\boldsymbol{f}_\mathfrak{e}, \boldsymbol{f}_\mathfrak{e}) + \sum_{j \in \mathrm{H}} \mathcal{J}_{\mathfrak{e}j}(\boldsymbol{f}_\mathfrak{e}, \boldsymbol{f}_j) \quad \text{and} \quad \mathcal{J}_i = \frac{1}{\varepsilon} \mathcal{J}_{i\mathfrak{e}}(\boldsymbol{f}_i, \boldsymbol{f}_\mathfrak{e}) + \sum_{j \in \mathrm{H}} \mathcal{J}_{ij}(\boldsymbol{f}_i, \boldsymbol{f}_j), \quad i \in \mathrm{H}. \tag{5}$$

Another important difference with standard multi-fluid models such as the one of Braginskii [16] is that both electron and heavy peculiar velocities are expressed in the same reference frame that is moving at the heavy particle bulk velocity $\boldsymbol{v}_\mathfrak{h}$.

Once the different scales are identified, the Chapman-Enskog method is applied. As done by Braginskii [16], the distribution functions are assumed to be a perturbed Maxwellian, at different temperatures for electrons and heavy particles, and the perturbation is expanded in successive orders of ε. This leads to a hierarchy of time scales that is presented in Table 1.

Table 1: Chapman-Enskog expansion and related hierarchy of time scales [4]

Order	**Time**	**Heavy particles**	**Electrons**
ε^{-2}	$t_\mathfrak{e}$		Thermalization $T_\mathfrak{e}$
ε^{-1}	$t_\mathfrak{h}$	Thermalization $T_\mathfrak{h}$	
ε^{0}	t	Euler Eqs.	0^{th}-order drift-diffusion Eqs.
ε	t/ε	Navier-Stokes Eqs.	1^{st}-order drift-diffusion Eqs.

Firstly, in time scale of order $t_\mathfrak{e}$, the electron population thermalizes at the temperature $T_\mathfrak{e}$. The electron distribution function is a Maxwellian and is obtained by solving the electron Boltzmann's equation at the order ε^{-2}. At order ε^{-1}, which corresponds to the time scale $t_\mathfrak{h}$, the heavy particle population thermalizes at the temperature $T_\mathfrak{h}$. At the zeroth order ε^0, which corresponds to the convective time scale, Euler's equations for heavy particle and first-order drift diffusion for electrons are obtained. Finally, at the last order ε investigated, corresponding to the diffusive time scale, we obtain the Navier-Stokes equations for heavy particle and second-order drift diffusion equations for electrons.

2.2. Governing equations for multicomponent plasma

Following the hierarchy presented in Table 1, one can obtain the macroscopic set of equations by taking moments. We stress the fact that the resulting multicomponent model is very different from the multi-fluid model of Braginskii [16]—while still capturing the same physics—for two reasons: first, the hierarchy of scales is different and, second, the distribution function of the electrons is a perturbed Maxwellian that is centered at the heavy particle bulk velocity instead of considering a different bulk velocity for the electrons. The set of macroscopic equations are presented below.

First, the mass conservation equation for the species α reads

$$\partial_t \rho_\alpha + \boldsymbol{\partial_x} \cdot \Big(\rho_\alpha(\boldsymbol{v}_\mathfrak{h} + \boldsymbol{V}_\alpha)\Big) = 0, \quad \alpha \in \{\mathfrak{e}, \mathrm{H}\}, \tag{6}$$

where $\rho_\mathfrak{e}$ is the density of electron, ρ_i, $i \in \mathrm{H}$, is the density of each heavy particle, $\boldsymbol{v}_\mathfrak{h}$ is the heavy particle hydrodynamic velocity that has been chosen as the velocity reference frame, $\boldsymbol{V}_\mathfrak{e}$ is the electron diffusion velocity, $\boldsymbol{V}_i$, $i \in \mathrm{H}$, is the heavy diffusion velocity in the heavy hydrodynamic reference frame.

Second, one momentum equation for all the particles within plasma is considered, as follows,

$$\partial_t(\rho_\mathfrak{h}\boldsymbol{v}_\mathfrak{h}) + \boldsymbol{\partial_x} \cdot \Big(\rho_\mathfrak{h}\boldsymbol{v}_\mathfrak{h} \otimes \boldsymbol{v}_\mathfrak{h} + p\mathbb{I}\Big) = -\boldsymbol{\partial_x} \cdot \boldsymbol{\Pi}_\mathfrak{h} + \mathfrak{n}\mathfrak{q}\boldsymbol{E} + \mathbf{I} \wedge \boldsymbol{B}. \tag{7}$$

Here, $p = p_\mathfrak{e} + p_\mathfrak{h}$ is the total pressure which is the sum of the partial pressure of electrons $p_\mathfrak{e}$ and heavy particles $p_\mathfrak{h}$, $\boldsymbol{\Pi}_\mathfrak{h}$ is the viscous stress tensor of heavy particles, $\rho_\mathfrak{h}$ is the total density of heavy particles, where $\mathfrak{n} = \mathfrak{n}_\mathfrak{e} + \mathfrak{n}_\mathfrak{h}$ is the density ($\mathfrak{n}_\mathfrak{e}$ the density of electrons, and $\mathfrak{n}_\mathfrak{h}$ the total density of heavy particles per unit volume), $\mathfrak{n}\mathfrak{q}$ is the total charge of the system defined by $\mathfrak{n}\mathfrak{q} = \mathfrak{n}_\mathfrak{e}\mathfrak{q}_\mathfrak{e} + \sum_{i\in\mathrm{H}} \mathfrak{n}_i\mathfrak{q}_i$, $\boldsymbol{E}$ is the electric field, and $\mathbf{I}$ is the total current density defined as

$$\mathbf{I} = \mathfrak{n}\mathfrak{q}\boldsymbol{v}_\mathfrak{h} + \boldsymbol{J}_\mathfrak{e} + \boldsymbol{J}_\mathfrak{h} = \mathfrak{n}\mathfrak{q}\boldsymbol{v}_\mathfrak{h} + \mathfrak{n}_\mathfrak{e}\mathfrak{q}_\mathfrak{e}\boldsymbol{V}_\mathfrak{e} + \sum_{i\in\mathrm{H}} \mathfrak{n}_i\mathfrak{q}_i\boldsymbol{V}_i, \tag{8}$$

where $\boldsymbol{J}_\mathfrak{h}$ is the heavy-particle conduction current density, $\boldsymbol{J}_\mathfrak{e}$ is the electron conduction current density, $\mathbf{I}$ is the total current density, and $\boldsymbol{B}$ is the magnetic field.

Third, the two equations (9) and (10) for the internal energies of electrons and ions read

$$\partial_t(\rho_\mathfrak{e}e_\mathfrak{e}) + \boldsymbol{\partial_x} \cdot (\rho_\mathfrak{e}e_\mathfrak{e}\boldsymbol{v}_\mathfrak{h}) + p_\mathfrak{e}\boldsymbol{\partial_x} \cdot \boldsymbol{v}_\mathfrak{h} + \boldsymbol{\partial_x} \cdot \boldsymbol{q}_\mathfrak{e} = \boldsymbol{J}_\mathfrak{e} \cdot \boldsymbol{E}' - \Delta E_\mathfrak{h}, \tag{9}$$

$$\partial_t(\rho_\mathfrak{h}e_\mathfrak{h}) + \boldsymbol{\partial_x} \cdot (\rho_\mathfrak{h}e_\mathfrak{h}\boldsymbol{v}_\mathfrak{h}) + (p_\mathfrak{h}\mathbb{I} + \boldsymbol{\Pi}_\mathfrak{h}) : \boldsymbol{\partial_x}\boldsymbol{v}_\mathfrak{h} + \boldsymbol{\partial_x} \cdot \boldsymbol{q}_\mathfrak{h} = \boldsymbol{J}_\mathfrak{h} \cdot \boldsymbol{E}' + \Delta E_\mathfrak{h}, \tag{10}$$

where $\rho_\mathfrak{e} e_\mathfrak{e}$ and $\rho_\mathfrak{h} e_\mathfrak{h}$ are the internal energies of electron and heavy-particles respectively, $\boldsymbol{q}_\mathfrak{e}$ and $\boldsymbol{q}_\mathfrak{h}$ are the electron and heavy particle heat fluxes, respectively, $\boldsymbol{E}' = \boldsymbol{E} + \boldsymbol{v}_\mathfrak{h} \wedge \boldsymbol{B}$ is the electric field in the heavy particle reference frame, $\Delta E_\mathfrak{h}$ is the familiar collisional Jean's relaxation term between the internal energy of electrons and heavy particles, $\boldsymbol{J}_\mathfrak{h} \cdot \boldsymbol{E}'$ and $\boldsymbol{J}_\mathfrak{e} \cdot \boldsymbol{E}'$ are respectively the power that is developed by the heavy particles and electrons current density.

By summing up the equations of the internal energies, i.e., Eq. (9) and Eq. (10), and the equation of kinetic energy, the equation of total energy can be obtained, as follows,

$$\partial_t \mathcal{E} + \boldsymbol{\partial_x} \cdot \Big((\mathcal{E} + p) \boldsymbol{v}_\mathfrak{h} \Big) + \boldsymbol{\partial_x} \cdot (\boldsymbol{\Pi}_\mathfrak{h} \cdot \boldsymbol{v}_\mathfrak{h}) + \boldsymbol{\partial_x} \cdot \Big(\boldsymbol{q}_\mathfrak{e} + \boldsymbol{q}_\mathfrak{h} \Big) = \mathbf{I} \cdot \boldsymbol{E}, \tag{11}$$

where $\mathcal{E} = \rho_\mathfrak{e} e_\mathfrak{e} + \rho_\mathfrak{h} e_\mathfrak{h} + 1/2 \rho_\mathfrak{h} \boldsymbol{v}_\mathfrak{h}^2$ is the total energy and $\mathbf{I} \cdot \boldsymbol{E}$ is the power developed by the electromagnetic field.

Only one momentum equation is considered in the model. Nevertheless, the different dynamics of the species are captured by the diffusion velocities $\boldsymbol{V}_\alpha$, $\alpha \in \{\mathfrak{e}, \mathrm{H}\}$. For the sake of brevity, the detailed expressions of the diffusive fluxes and the corresponding transport coefficients are not given here. In the multicomponent case, the general expressions of the diffusion velocities and heat fluxes for electrons and heavy particles, the corresponding second order drift diffusion terms for electrons and the viscous stress tensor can be found respectively in Eq. (5.15) and Eq. (5.33), Eq. (5.20) and Eq. (5.39), Eq. (5.51) and Eq. (5.52) and Eq. (5.37) in Graille et al. [4]. In the fully-ionized plasma case, simplified expressions of the diffusive fluxes can be obtained. The latter are provided in the following Section 2.3.

The system of equations (6)-(11) is coupled to the set of Maxwell's equations (12)

$$\boldsymbol{\partial_x} \cdot \boldsymbol{E} = \frac{\mathrm{nq}}{\varepsilon_0}, \quad \boldsymbol{\partial_x} \cdot \boldsymbol{B} = 0, \quad \partial_t \boldsymbol{B} = -\boldsymbol{\partial_x} \wedge \boldsymbol{E}, \quad \text{and} \quad \boldsymbol{\partial_x} \wedge \boldsymbol{B} = \mu_0 \mathbf{I} + \mu_0 \varepsilon_0 \partial_t \boldsymbol{E} \tag{12}$$

where ε_0 is the vacuum permittivity and μ_0 the vacuum permeability. Even though the model does not assume charge neutrality, this assumption is valid when the scales of interest are much larger than the Debye length.

The governing equations (6)-(12) differ from the classical multi-fluid models [6, 7, 2, 3] that are used for partially-ionized plasmas. Whereas multi-fluid models consider one hydrodynamic velocity and one temperature for each species, the present model considers one hydrodynamic velocity for the heavy species and two temperatures, one for the heavy species and another one for the electrons.

From a numerical point of view, this system is simpler than the multi-fluid equations as it does not contain the stiffness that is associated to the different velocities of each species and to the collisional relaxation terms. In particular, the electron momentum equation, which introduces very fast dynamics, is not solved as electrons are represented by the drift-diffusion approximation. Nevertheless, the effect of the collisions as well as the different dynamics of each species are still captured in the model through the diffusive fluxes. Additionally, this model can be used for both partially- and fully-ionized plasmas. On the other hand, the model of Braginskii is formally difficult to extend for partially-ionized reacting plasmas as the collisional integrals are difficult to be solved when the masses of the particles are of the same order and the Maxwellian distributions are shifted in different bulk velocities. Recently, Zhdanov & Stepanenko [18, 19] have proposed a model that tackles partially-ionized reactive plasmas, that extend the work of Braginskii. The present work can be considered complementary to the previous literature.

In conclusion, the present model has an extended range of validity for partially- and fully-ionized, weakly- and highly-magnetized plasmas, multicomponent mixtures. Additionally, an entropy inequality combined to Onsager reprocity relations for the transport properties, so the second law of thermodynamics is verified [4]. Finally, the proposed model is valid in all regimes representative of the Sun atmosphere and can be used for representing magnetic reconnection configurations under such conditions.

2.3. Fully-ionized plasma case

We focus on a fully-ionized plasma composed of $S = \{\mathfrak{e}, H^+\}$, considering scales which are much larger than the Debye length, in a non-relativistic framework. Under these assumptions, the heavy diffusion velocity is null $\boldsymbol{V}_\alpha = 0, \alpha \in \mathrm{H}$, and the global charge is nul $\mathfrak{nq} = 0$, so the total current density Eq. (8) is equal to the electron current density. Then, in the momentum equation (7), the Lorentz force can be written as a flux by using Faraday's law leading to a conservative expression of the momentum equation. Finally, by using Poynting's theorem, the total energy equation from Eq. (11) can be rewritten into a conservative form as well.

In the following, as we have only hydrogen ions as heavy particles, $\mathfrak{h}$ is denoted as H^+. We normalize the governing equations Eqs. (6-12) with a reference length L_0, reference density ρ_0 equal to the density of H^+, and a reference magnetic field B_0. All the reference magnitudes are computed using a combination of these reference dimensions. For the sake of clarity, the following quantities are written in a dimensionless form. The governing equations coupled to the set of Maxwell's equations read

$$\partial_t \rho_\alpha + \boldsymbol{\partial_x} \cdot (\rho_\alpha \boldsymbol{v}_\mathfrak{h}) = 0, \quad \alpha \in \{\mathfrak{e}, \mathfrak{h}\} \tag{13}$$

$$\partial_t(\rho_\mathfrak{h} \boldsymbol{v}_\mathfrak{h}) + \boldsymbol{\partial_x} \cdot \Big(\rho_\mathfrak{h} \boldsymbol{v}_\mathfrak{h} \otimes \boldsymbol{v}_\mathfrak{h} + (p_\mathfrak{e} + p_\mathfrak{h} + \tfrac{1}{8\pi}|\boldsymbol{B}|^2)\mathbb{I} - \tfrac{1}{8\pi}\boldsymbol{B} \otimes \boldsymbol{B}\Big) + \boldsymbol{\partial_x} \cdot \boldsymbol{\Pi}_\mathfrak{h} = 0, \tag{14}$$

$$\partial_t \mathcal{E} + \boldsymbol{\partial_x} \cdot \Big((\mathcal{E} + p_\mathfrak{e} + p_\mathfrak{h})\boldsymbol{v}_\mathfrak{h} + \tfrac{1}{4\pi}\boldsymbol{E} \wedge \boldsymbol{B}\Big) + \boldsymbol{\partial_x} \cdot (\boldsymbol{\Pi}_\mathfrak{h} \cdot \boldsymbol{v}_\mathfrak{h}) + \boldsymbol{\partial_x} \cdot (\boldsymbol{q}_\mathfrak{e} + \boldsymbol{q}_\mathfrak{h}) = 0, \tag{15}$$

$$\partial_t(\rho_\mathfrak{e} e_\mathfrak{e}) + \boldsymbol{\partial_x} \cdot (\rho_\mathfrak{e} e_\mathfrak{e} \boldsymbol{v}_\mathfrak{h}) + p_\mathfrak{e} \boldsymbol{\partial_x} \cdot \boldsymbol{v}_\mathfrak{h} + \boldsymbol{\partial_x} \cdot \boldsymbol{q}_\mathfrak{e} - \boldsymbol{J}_\mathfrak{e} \cdot \boldsymbol{E}' + \Delta E_\mathfrak{h} = 0, \tag{16}$$

$$\boldsymbol{\partial_x} \cdot \boldsymbol{E} = 0, \quad \boldsymbol{\partial_x} \cdot \boldsymbol{B} = 0, \quad \partial_t \boldsymbol{B} = -\boldsymbol{\partial_x} \wedge \boldsymbol{E}, \quad \tfrac{1}{4\pi}\boldsymbol{\partial_x} \wedge \boldsymbol{B} = \mathbf{I} = \boldsymbol{J}_\mathfrak{e}, \tag{17}$$

where $\gamma = 5/3$, $p_\mathfrak{e} = (\gamma - 1)\rho_\mathfrak{e} e_\mathfrak{e} = \Big(m_\mathfrak{h}/m_\mathfrak{e}\Big)\rho_\mathfrak{e} T_\mathfrak{e}$, and $p_\mathfrak{h} = (\gamma - 1)\rho_\mathfrak{h} e_\mathfrak{h} = \rho_\mathfrak{h} T_\mathfrak{h}$. After some algebra, the transport fluxes and the collisional Jean's relaxation term read

$$\boldsymbol{\Pi}_\mathfrak{h} = -\eta_\mathfrak{h}\Big(\boldsymbol{\partial_x} \boldsymbol{v}_\mathfrak{h} + (\boldsymbol{\partial_x} \boldsymbol{v}_\mathfrak{h})^\top - \tfrac{2}{3}(\boldsymbol{\partial_x} \cdot \boldsymbol{v}_\mathfrak{h})\mathbb{I}\Big), \qquad \Delta E_\mathfrak{h} = \tfrac{1}{\tau}\Big(\rho_\mathfrak{e} e_\mathfrak{e} - \rho_\mathfrak{h} e_h\Big), \tag{18}$$

$$\boldsymbol{q}_\mathfrak{e} = -\bar{\bar{\lambda}}_\mathfrak{e} \boldsymbol{\partial_x} T_\mathfrak{e} + \tfrac{1}{\omega_\mathfrak{e} t_0}(p_\mathfrak{e} \bar{\bar{\chi}}_\mathfrak{e} + \rho_\mathfrak{e} h_\mathfrak{e}) \tfrac{1}{4\pi\rho_\mathfrak{e}} \boldsymbol{\partial_x} \wedge \boldsymbol{B}, \qquad \boldsymbol{q}_\mathfrak{h} = -\lambda_\mathfrak{h} \boldsymbol{\partial_x} T_\mathfrak{h}, \tag{19}$$

$$\boldsymbol{V}_\mathfrak{e} = \tfrac{1}{4\pi\rho_\mathfrak{e}} \boldsymbol{\partial_x} \wedge \boldsymbol{B}, \tag{20}$$

where $t_0 = L_0/v_0$ and $\omega_\mathfrak{e}$ are respectively the reference time and the cyclotron frequency of electrons, $\bar{\bar{\lambda}}_\mathfrak{e}$, $\bar{\bar{\chi}}_\mathfrak{e}$ are the dimensionless electron thermal conductivity and electron thermal diffusion ratio tensors, $\lambda_\mathfrak{h}$, $\eta_\mathfrak{h}$ are the dimensionless heavy thermal conductivity and heavy viscosity, and τ is the dimensionless average collision time at which the energy transfer between the internal energy of electrons and heavy particles occurs. Then, similarly as in Wargnier *et al.* [13], an expression of the electric field $\boldsymbol{E}$ can be obtained by using Ampere's law and the definition of the current density:

$$\boldsymbol{E} = -\boldsymbol{v}_\mathfrak{h} \wedge \boldsymbol{B} + \bar{\bar{\eta}}_e \boldsymbol{J}_\mathfrak{e} + \frac{\boldsymbol{\partial_x} p_\mathfrak{e}}{\mathfrak{n}_\mathfrak{e} \mathfrak{q}_\mathfrak{e}} + \frac{p_\mathfrak{e}}{\mathfrak{n}_\mathfrak{e} \mathfrak{q}_\mathfrak{e}} \bar{\bar{\chi}}_\mathfrak{e} \boldsymbol{\partial_x} \ln T_\mathfrak{e}, \tag{21}$$

where $\bar{\bar{\eta}}_e$ is the electron resistivity tensor. The presented transport coefficients are computed using a spectral Galerkin method based on a third-order Laguerre-Sonine polynomials approximation, where the general expressions can be found in Scoggins *et al.* [20] and have been computed in conditions related to the Sun chromosphere in Wargnier *et al.* [13].

The presented model Eqs. (13)-(17) is a thermal non-equilibrium model. In this framework, the electron heat flux is anisotropic and depends on the direction of the magnetic field whereas the heavy heat flux and viscous stress tensor are isotropic. Source terms are involved in the equation of internal energy of electrons that can be decomposed as nonconservative and relaxation terms. The nonconservative terms such as $p_\mathfrak{e} \boldsymbol{\partial_x} \cdot \boldsymbol{v}_\mathfrak{h}$ or the power developed by the electromagnetic field $\boldsymbol{J}_\mathfrak{e} \cdot \boldsymbol{E}'$, are part of the thermal non-equilibrium process which tends to change the electronic temperature with respect to the temperature of the heavy particles. The contribution in Wargnier *et al.* [21], in the case of a simplified system without

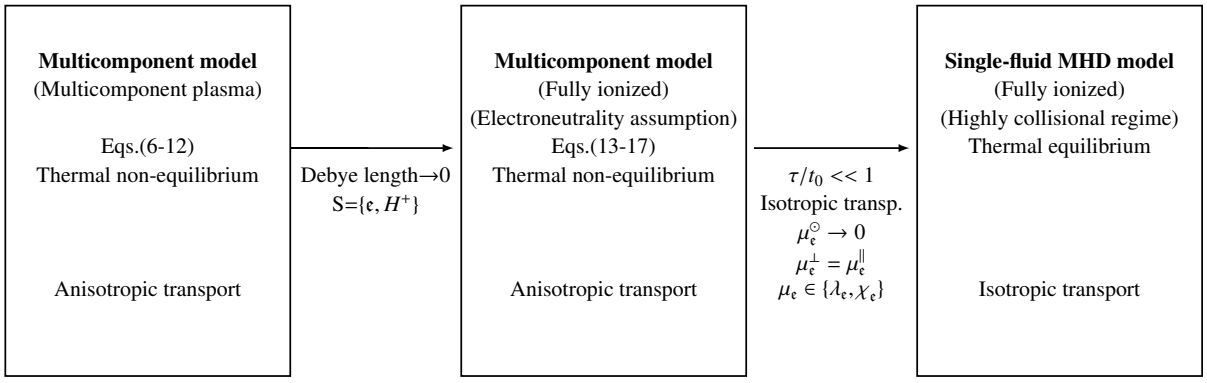

Figure 1: Link between the presented general multicomponent model from Eqs.(6-12), the simplified model from Eqs.(13-17) and the single-fluid MHD model, assuming that the structure of the transport system and the method used for computing the transport coefficients is the same between the two models.

considering electromagnetic field, has shown that the nonconservative terms play a major role in the structure of shock waves, in particular for the jump conditions. The strategy for solving this simplified problem can be extended to the case coupled to the electromagnetic field, and is currently being studied.

In the presented model, the source term $\Delta E_{\mathfrak{h}}$, present in the equation of internal energy of electron, tends to relax the system towards a state of thermal equilibrium between the electrons and the heavy particles. This relaxation is related to the parameter τ, which is the characteristic time of collision between electrons and heavy particles. Physically, if this characteristic collision time is small enough compared to the characteristic reference time, we have a thermal equilibrium state. If not, the power generated by the electromagnetic field $\boldsymbol{J}_{\mathfrak{e}} \cdot \boldsymbol{E}'$ dominates the dynamic of the internal energy of electron, the electronic temperature becomes different from the temperature of the heavy ones, we get a thermal non-equilibrium state.

If we consider all the typically models used in solar physics applications, we have the multi-fluid models and the single fluid MHD model [22]. In this work, we focus only on the comparison between the multicomponent model and the single fluid MHD model. The latter is a model in thermal equilibrium between heavy particles and electrons. Unlike the system presented previously, the system is conservative, without source terms, in which the structure of the diffusive terms, i.e heat fluxes and viscous stress tensor, is in general isotropic. In this framework, the system considered by Wray *et al.* [22] does not depend on the characteristic collision time and does not represent regimes where there is thermal non-equilibrium. Finally, Fig. 1 represents the link between the presented general multicomponent model defined by Eqs.(6)-(12), the simplified model given by Eqs.(13)-(17) and the single-fluid MHD model, if the structure of the transport systems as well as the method used for computing the transport coefficients (spectral Galerkin method) are identical between the three models. For the sake of clarity, in this work, we focus only on the case where the transport systems and the corresponding method used for computing the transport coefficients is identical in both models.

Finally, on the one hand, we have a model which allows to describe all collisional regimes, in equilibrium or thermal non-equilibrium, through source terms of relaxation type. On the other hand, we have a conservative model valid only in thermal equilibrium cases, i.e., in highly collisional regimes. Consequently, a comparison between the two models would be relevant to understand the difference between each other, in several collisional regimes for magnetic reconnection under Sun atmosphere conditions. Finally, the possibility of being able to represent all these regimes is particularly important in the solar atmosphere, since we can find highly or weakly collisional regimes in different parts of the solar atmosphere.

3. Numerical strategy

Using a massively parallel code called CanoP, we implement our simplified model and the single fluid MHD model using a second order Kurganov-Tadmor scheme [23] combined to a second order TVD Runge-Kutta scheme for the space and time discretization. The CanoP code is coupled to a library called p4est. This provides a parallel scalable implementation of cell-based adaptive mesh refinement for distributed memory computing systems. For computing the presented transport properties in both models, we use the Multicomponent Thermodynamic And Transport properties for Ionized gases in C++ (MUTATION++) library designed to provide efficient algorithms for the computation of various properties important also in the fields of hypersonics and combustion Computational Fluid Dynamics (CFD) including thermodynamic properties, multicomponent transport properties, finite rate chemistry in thermal non-equilibrium and a highly robust multiphase equilibrium solver. We verify the implementation of the convective fluxes, divergence cleaning method through a series of classical test cases used for MHD systems. A more detailed description of the numerical methods and performance of the code used in 2D or 3D, in the context of Adaptive Mesh Refine (AMR), can be found in Wargnier *et al.* [14].

3.1. Description of the CanoP *code,* p4est *and* MUTATION ++ *libraries*

The p4est library defines a mesh as a collection of interconnected adaptive octrees (hence the name p4est). Octrees are efficiently represented and stored with a very low memory footprint; only cells' meta-data are used in p4est. AMR mesh topology is completely decoupled from any application-specific numerical data. Given that p4est is able to build a unique cell numbering accross all processors using a space-filling curve technique (here the z-curve Morton order, see Fig. 2), the main features of the library is to use this functionality to (re-)partition or re-distribute the cells meta-data over all the MPI computing nodes, as well as to locally modify a mesh by refining or coarsening some cells, that are identified according to a user defined constraint (that can be purely geometrical or user-data dependent).

As the p4est library is a generic cell-based AMR mesh management tool, it is completely independent of the specific details of numerical schemes used to solve a given PDE problem. CanoP is an applicative software layer built on top of the mesh manager library p4est, that enables to solve systems of conservation laws with finite volume discretization schemes on 2D and 3D adaptive grids [9]. The CanoP software package has been designed to be a versatile application developpement framework. Several finite volume-like numerical schemes have been implemented to target e.g. compressible two-phase flows [9] (like air-water systems with high density ratio), dispersive-phase flows [10]. A second-order Godunov finite volume scheme for single-phase flow has been used to study angular momentum transport in hydrodynamical accretion disk setups. In the present work, we introduced a new application to magneto-hydrodynamics by adapting a cell-centered Kurganov-Tadmor scheme in the context of cell-based AMR.

When developping a new application, i.e., a new numerical scheme implementation, one first needs to define a data structure holding relevant physics quantities in each cell that are used to represent the fluid state, which are updated in time by the numerical scheme discretization. All that is left to the application developper is to specify the computing kernels in terms of local cell-wise operators, also named callback functions. These callback functions are passed to p4est internal routines which iterate over the AMR mesh cells. One major advantage of using the CanoP software package is that it only needs to focus on the numerical scheme operator, i.e. in the context of finite volume discretization, how to compute fluxes at the cells interfaces and how to update the fluid state variables inside each cell. The CanoP framework aims then at facilitating the integration of new finite volume applications, or new finite volume features, such as high-order schemes, low-Mach number solvers, which are under development.

In order to perform the computation of the transport properties, we use another library called MUTATION++[12, 20]. This library is coupled to the software CanoP [9], which gives the possibility to compute all the transport properties of the general multicomponent model with high accuracy, for any plasma mixture in thermal or chemical non-equilibrium. The used method is a spectral Galerkin method

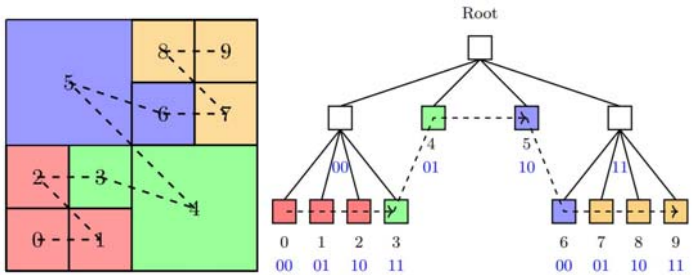

Figure 2: Left: Adaptively refined square domain. Mesh and z-order curve. Right : The corresponding representation of the domain using a quadtree.

based on a third order Laguerre Sonine polynomial approximation. This method has been detailed in the literature (e.g., [24, 25, 17, 26]) and used for solar physics applications in Wargnier *et al.* [13].

3.2. Numerical scheme

In the following, we consider a hyperbolic divergence cleaning method described in [27, 28], which is a Generalized Lagrange Multiplier (GLM) with a mixed hyperbolic-parabolic correction to deal with the magnetic field incompressibility condition. The considered system Eqs.(13-17) can be written as follows,

$$\partial_t \mathcal{U} + \boldsymbol{\partial_x} \cdot \mathcal{F}(\mathcal{U}) + \boldsymbol{\partial_x} \cdot (\mathcal{D}(\mathcal{U})\boldsymbol{\partial_x}\mathcal{U}) = \mathcal{S}(\mathcal{U}, \boldsymbol{\partial_x}\mathcal{U}), \tag{22}$$

where $\mathcal{U} \in \mathbb{R}^{11}$, $\mathcal{F}(\mathcal{U}) \in \mathbb{R}^{3\times 11}$, $\mathcal{D}(\mathcal{U}) \in \mathbb{R}^{3\times 3\times 11}$ and $\mathcal{S}(\mathcal{U}, \boldsymbol{\partial_x}\mathcal{U}) \in \mathbb{R}^{3\times 11}$ are respectively the conservative variables, the convective fluxes, the diffusive fluxes and the source terms defined by

$$\begin{aligned}
\mathcal{U} &= \Big(\rho_{\mathfrak{e}},\ \rho_{\mathfrak{h}},\ \rho_{\mathfrak{h}}\boldsymbol{v}_{\mathfrak{h}}^T,\ \mathcal{E},\ \rho_{\mathfrak{e}}e_{\mathfrak{e}},\ \boldsymbol{B}^T,\ \psi\Big)^T,\\
\mathcal{F}(\mathcal{U}) &= \Big(\rho_{\mathfrak{e}}\boldsymbol{v}_{\mathfrak{h}},\ \rho_{\mathfrak{h}}\boldsymbol{v}_{\mathfrak{h}},\ \rho_{\mathfrak{h}}\boldsymbol{v}_{\mathfrak{h}}\otimes\boldsymbol{v}_{\mathfrak{h}} + \Big(p_{\mathfrak{e}} + p_{\mathfrak{h}} + \tfrac{1}{8\pi}|\boldsymbol{B}|^2\Big)\mathbb{I} - \tfrac{1}{8\pi}\boldsymbol{B}\otimes\boldsymbol{B},\\
&\qquad (\mathcal{E} + p_{\mathfrak{e}} + p_{\mathfrak{h}})\boldsymbol{v}_{\mathfrak{h}} + \tfrac{1}{4\pi}\boldsymbol{E}\wedge\boldsymbol{B},\ \rho_{\mathfrak{e}}e_{\mathfrak{e}}\boldsymbol{v}_{\mathfrak{h}},\ \mathbb{I}\wedge\boldsymbol{E} + \psi\mathbb{I},\ c_h^2\boldsymbol{B}\Big)^T,\\
\mathcal{D}(\mathcal{U})\boldsymbol{\partial_x}\mathcal{U} &= \Big(0_3,\ 0_3,\ \boldsymbol{\Pi}_{\mathfrak{h}},\ \boldsymbol{\Pi}_{\mathfrak{h}}\cdot\boldsymbol{v}_{\mathfrak{h}} + \boldsymbol{q}_{\mathfrak{e}} + \boldsymbol{q}_{\mathfrak{h}},\ \boldsymbol{q}_{\mathfrak{e}},\ 0_{3\times 3},\ 0_3\Big)^T,\\
\mathcal{S}(\mathcal{U}, \boldsymbol{\partial_x}\mathcal{U}) &= \Big(0,\ 0,\ 0_3^T,\ 0,\ -p_{\mathfrak{e}}\boldsymbol{\partial_x}\cdot\boldsymbol{v}_{\mathfrak{h}} + \boldsymbol{J}_{\mathfrak{e}}\cdot\boldsymbol{E}' - \Delta E_{\mathfrak{h}},\ 0_3^T,\ -\frac{c_h^2}{c_p^2}\psi\Big)^T,
\end{aligned} \tag{23}$$

where ψ is a scalar which couples the divergence constraint equation to Faraday's law, c_h is a parameter related to the hyperbolic correction responsible for the propagation of the divergence errors, and c_p is a parabolic correction for the damping of monopoles. The value of c_h and c_p will be described in the next section.

The convective fluxes are computed using a Kurganov-Tadmor scheme [23], which is a Riemann-solver-free, second-order, high-resolution scheme that uses a Monotonic Upwind Scheme for Conservation Laws (MUSCL) reconstruction, combined to a van Albada [29] slope limiter function. The diffusive fluxes are computed using a central difference approximation compatible with the Kurganov-Tadmor scheme [23]. A Total Variation Diminishing (TVD) second order Runge-Kutta scheme has been used for the time integration. The relaxation terms are computed using a second order implicit scheme combined to a splitting operator technique [30]. The nonconservative terms are computed as an average at the middle of each cell where the gradients are taken as a second order central scheme.

It is important to note that in Wargnier *et al.* [21], it has been shown that, in the presence of strong gradients or shock waves, a naive consistent discretization of the nonconservative terms may lead to

additional artificial numerical jumps due to the numerical dissipation of the numerical scheme. A specific numerical treatment of the nonconservative product may be required in order to properly capture shock waves. It is particularly relevant if the level of resolution necessary to capture these waves is too coarse. In [21] we have focused so far on a simplified model. It would be necessary to extend this strategy by considering the electromagnetic field.

The single-fluid MHD model [22] has been implemented by using the same numerical scheme that is used for the multicomponent model. In this case, no source terms need to be implemented.

3.3. Verification

In order to verify the implementation of the two models, we have run test cases that are used as benchmarks in ideal MHD simulations. In the following, we will verify the implementation of the convective fluxes of the two models. In the case of the multicomponent model, we do not solve for the full system defined by Eq. (23). Alternatively, we solve for the same convective part without diffusive and source terms (except the component that is used for the divergence free constraint). For the purpose of the paper, we show results only for two dimensional configurations. Nevertheless, similar results have been obtained in one and three dimensional configurations, with and without adaptive mesh refinement [14]. A second-order time and space discretization has been verified and tested with uniform 256×256 cells. More details of the accuracy analysis and relevance of the presented scheme are given in [14].

We verify the ability of the proposed numerical solver to tackle MHD shocks, shock-shock interactions, and the divergence-free constraint. In order to perform the validation, we focus on two classical test cases: the Orszag-Tang (OT) configuration [31], and the rotor MHD problem. On the one hand, the Orszag-Tang configuration is based on a transition to 2D supersonic MHD turbulence and is used to validate MHD solvers. On the other hand, the rotor MHD problem is based on the evolution of a 2D strong torsional Alfvén wave in ideal MHD, described by Balsara & Spicer [32]. The rotor MHD problem is a high-density disk that is rotating at large velocity inside a constant pressure and constant magnetic field in the x direction. In both cases, we consider a domain where $(x, y) \in [0, 1] \times [0, 1]$ with periodic boundary conditions in both directions, with a uniform mesh 256×256. The initial conditions for the Orszag-Tang test case $\mathcal{U}_{\rm OT}(t = 0)$ and the rotor MHD test case $\mathcal{U}_{\rm r}(t = 0)$ are

$$\mathcal{U}_{\rm OT}(t=0) = \left(\frac{m_{\mathfrak{e}}}{m_{\mathfrak{h}}}\rho_{\mathfrak{h}},\ \gamma\frac{5}{12\pi},\ -\rho_{\mathfrak{h}} sin(2\pi y),\ \rho_{\mathfrak{h}} sin(2\pi x),\ \mathcal{E}_{\rm OT},\ \frac{5}{24\pi(\gamma-1)},\ -sin(2\pi y),\ sin(4\pi x),\ 0\right)^T, \tag{24}$$

and

$$\begin{cases} r \geq r_0, & \mathcal{U}_{\rm r}(t=0) = \left(\frac{m_{\mathfrak{e}}}{m_{\mathfrak{h}}}\rho_{\mathfrak{h}},\ 10,\ -\frac{2\rho_{\mathfrak{h}}(y-y_c)}{r_0},\ \frac{2\rho_{\mathfrak{h}}(x-x_c)}{r_0},\ \mathcal{E}_{\rm r},\ \frac{1}{2(\gamma-1)},\ 5,\ 0,\ 0\right)^T, \\ r < r_0, & \mathcal{U}_{\rm r}(t=0) = \left(\frac{m_{\mathfrak{e}}}{m_{\mathfrak{h}}}\rho_{\mathfrak{h}},\ 1+9f(r),\ -\frac{2\rho_{\mathfrak{h}}(y-y_c)f(r)}{r},\ \frac{2\rho_{\mathfrak{h}}(x-x_c)f(r)}{r},\ \mathcal{E}_{\rm r},\ \frac{1}{2(\gamma-1)},\ 5,\ 0,\ 0\right)^T, \\ r < r_1, & \mathcal{U}_{\rm r}(t=0) = \left(\frac{m_{\mathfrak{e}}}{m_{\mathfrak{h}}}\rho_{\mathfrak{h}},\ 1,\ 0,\ 0,\ \mathcal{E}_{\rm r},\ \frac{1}{2(\gamma-1)},\ 5,\ 0,\ 0\right)^T. \end{cases} \tag{25}$$

Here, $\mathcal{E}_{\rm OT} = 5/12\pi(\gamma-1) + 1/2\rho_{\mathfrak{h}}|\boldsymbol{v}_{\mathfrak{h}}|^2 + |B|^2/8\pi$ and $\mathcal{E}_{\rm r} = 1/(\gamma-1) + 1/2\rho_{\mathfrak{h}}|\boldsymbol{v}_{\mathfrak{h}}|^2 + 25/8\pi$, the adiabatic constant is $\gamma = 5/3$, the radius is $r = \sqrt{(x-x_c)^2 + (y-y_c)^2}$, $r_0 = 0.115$ and $r_1 = 0.1$, the center of the disk is located at $y_c = x_c = 0.5$, the ratio $m_{\mathfrak{e}}/m_{\mathfrak{h}} = 10^{-3}$. We choose a $CFL = 0.7$. In order to maintain the divergence free constraint, we choose $c_h = CFL\Delta x/\Delta t$ and $c_p = \sqrt{0.18 c_h}$, chosen as in [28]. The two test cases are run until $t = 0.5$ for the Orszag-Tang test case and until $t = 0.2$ for the rotor MHD problem.

Fig. 3 shows the distribution of the density $\rho_{\mathfrak{h}}$ at $t = 0.25$ and $t = 0.5$ for the OT test case. The results obtained show agreement with MHD solutions from literature [34, 35]. We have obtained also good agreement with the other conservative variables. Besides, in Fig. 4, the total pressure p distribution along the lines $y = 0.4277$ and $y = 0.3125$ at $t = 0.5$ are in good agreement with the solution obtained by

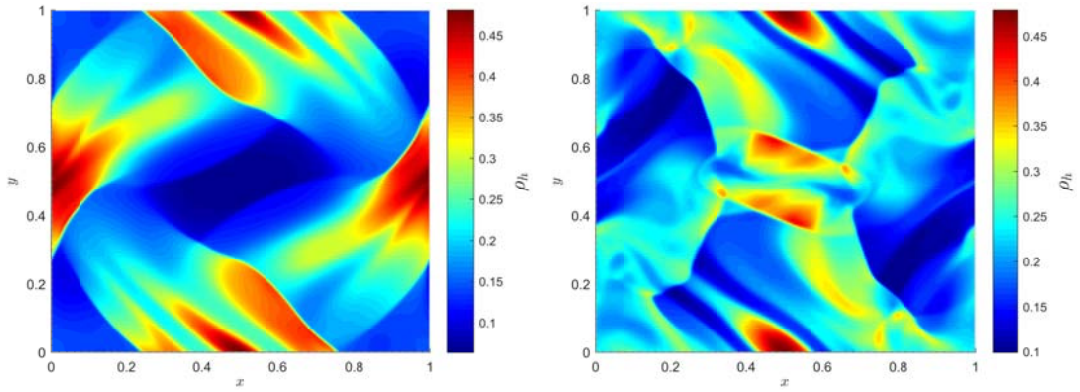

(a) Density distribution $\rho_\mathfrak{h}$ at $t = 0.25$. (b) Density distribution $\rho_\mathfrak{h}$ at $t = 0.5$.

Figure 3: Density $\rho_\mathfrak{h}$ distribution for the Orszag-Tang test case at $t = 0.25$ and $t = 0.5$ on a uniform mesh 256×256.

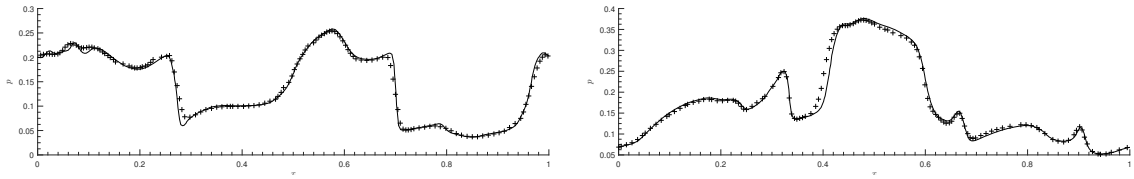

Figure 4: Total pressure p distribution at $y = 0.3125$ (left) and $y = 0.4277$ (right), at $t = 0.5$. Results from our simulation in full line on a uniform mesh 256×256, and + results from Londrillo et al. [33] on a uniform mesh 192×192.

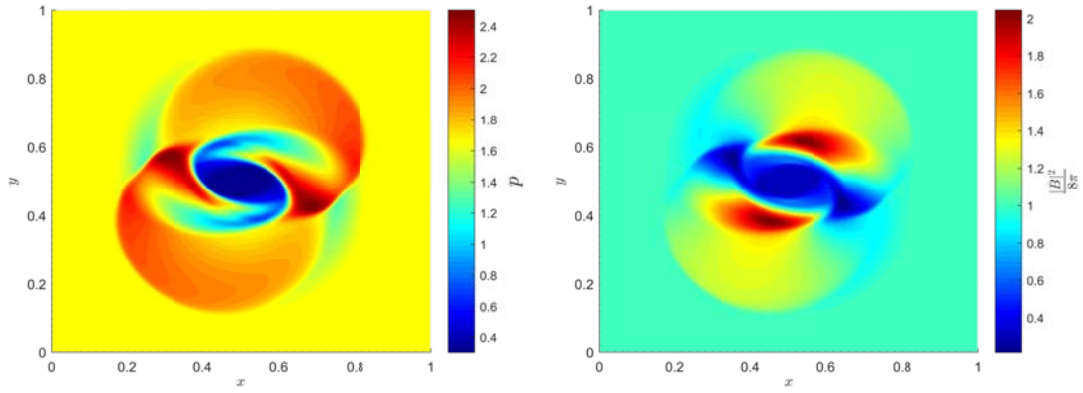

(a) Total pressure distribution p at $t = 0.15$. (b) Magnetic energy distribution at $t = 0.15$.

Figure 5: Total pressure p and magnetic energy distribution in the Rotor MHD test case at $t = 0.15$ and on a mesh 256×256.

Londrillo et al. [33] where a uniform mesh 192×192 has been used, and the divergence free constraint is discretized using a reconstruction method for high order upwind schemes based on the magnetic field potential.

In Fig. 5, we show results for the total pressure p and magnetic energy at $t = 0.15$ for the rotor MHD problem. The results are showing good agreement with the common solution, presented for example in [35]. Similar results have been obtained for the other conservative variables.

In the presented test cases, we have been able to verify the level of accuracy and ability to capture

discontinuities of the presented scheme, the implementation of the convective fluxes, and the ability to maintain the divergence free constraint for the multicomponent model as well as the single fluid MHD model. After the verification performed in this section, we set a two dimensional magnetic reconnection test case under Sun atmosphere conditions, and compare the single-fluid MHD model with the multicomponent model.

4. Results for a 2D magnetic reconnection in a fully ionized plasma

In this section, the results are presented using two models for a fully ionized plasma $S = \{\mathfrak{e}, H^+\}$: (1) the full multicomponent plasma model from Eq. (23), which includes diffusion fluxes and source terms and (2) a reference single-fluid MHD model with isotropic diffusive fluxes [22]. First, the comparison is performed in a two dimensional magnetic reconnection configuration under Sun photosphere conditions. In a second study, in order to analyze the influence of the thermal non-equilibrium process on the dynamic of this magnetic reconnection, we will study the same test case where we will artificially change the value of the parameter τ (mean collision time between electron and H^+) in the multicomponent model, in order to be in a weakly collisional regime. Finally, the idea is to see for this case of magnetic reconnection, the difference between the two models in various collisional regimes.

We choose a reference length of $L^* = 100$ m and characteristic properties of the Sun photosphere such as a reference temperature $T^* = 8000$ K, a total pressure $P^* = 10^4$ Pa, a reference density of heavy particles H^+ such as $\rho^* = 7.573 \times 10^{-5}\, kg.m^{-3}$, and a strong magnitude of magnetic field such as $B^* = 1000$ G. Using `MUTATION++` library, the mean collision time between electron and H^+ is found to be $\tau^* = 4.81 \times 10^{-12}$ s. The reference timescale t^* is also defined as $t^* = L^*/v^*$, where v^* is the characteristic speed computed as the reference speed of sound. Under these conditions, we have $\tau^*/t^* \approx 10^{-9}$, which implies that we are in a highly collisional regime. Then, we normalize all the quantities with these reference values. The transport properties are computed using the `MUTATION++` library and are presented in the following table 2; where the transport coefficients of the single-fluid MHD model are shown as well as the parallel and perpendicular components of the tensor of each electron transport coefficients.

Table 2: Transport coefficients used both in the multicomponent and single fluid MHD model

$\eta_\mathfrak{e}^\parallel$ [$\Omega.m$]	$\eta_\mathfrak{h}$ [$Pa.s$]	$\lambda_\mathfrak{h}\left[W.m^{-1}.K^{-1}\right]$	$\lambda_\mathfrak{e}^\parallel\left[W.m^{-1}.K^{-1}\right]$	$\chi_\mathfrak{e}^\parallel[-]$	
3.378×10^{-4}	4.45×10^{-7}	0.0138	0.3514	0.644	
$\eta_\mathfrak{e}^\perp$ [$\Omega.m$]	$\eta_\mathfrak{e}^\odot$ [$\Omega.m$]	$\lambda_\mathfrak{e}^\perp\left[W.m^{-1}.K^{-1}\right]$	$\lambda_\mathfrak{e}^\odot\left[W.m^{-1}.K^{-1}\right]$	$\chi_\mathfrak{e}^\perp[-]$	$\chi_\mathfrak{e}^\odot[-]$
3.338×10^{-4}	-2.85×10^{-6}	0.3506	-0.0153	0.6429	-0.02

Initially, we consider a magnetic field configuration consisting of a double 2D Harris current sheet [36, 2, 3]. The configuration contains a small perturbation for the magnetic field in the center of each current sheet in order to initiate the reconnection. The total pressure is balanced by the magnetic pressure, and the initial velocity field is set to zero. We consider a domain where $(x, y) \in [0, 1]\times[0, 1]$ with periodic boundary conditions in all the directions, with a uniform mesh 256×256 where the current sheets are located at $y = 1/4$ and $y = 3/4$. Thus, in the subdomain $x \in [0, 1]$ and $y \in [0, 1/2]$, the initial conditions for the multicomponent model are $\mathcal{U}(t = 0) = \mathcal{U}_0$

$$\mathcal{U}_0 = \left(\frac{m_\mathfrak{e}}{m_\mathfrak{h}}\overline{\rho_\mathfrak{h}},\ \left(1 + \frac{\psi_0}{\cosh^2\left(\frac{y-1/4}{\delta}\right)}\right),\ 0,\ 0,\ \frac{p}{\gamma-1} + \frac{|B|^2}{8\pi},\ \frac{p}{2(\gamma-1)},\ B_0 \tanh\left(\frac{y-1/4}{\delta}\right) - B'_x,\ B'_y,\ 0\right), \tag{26}$$

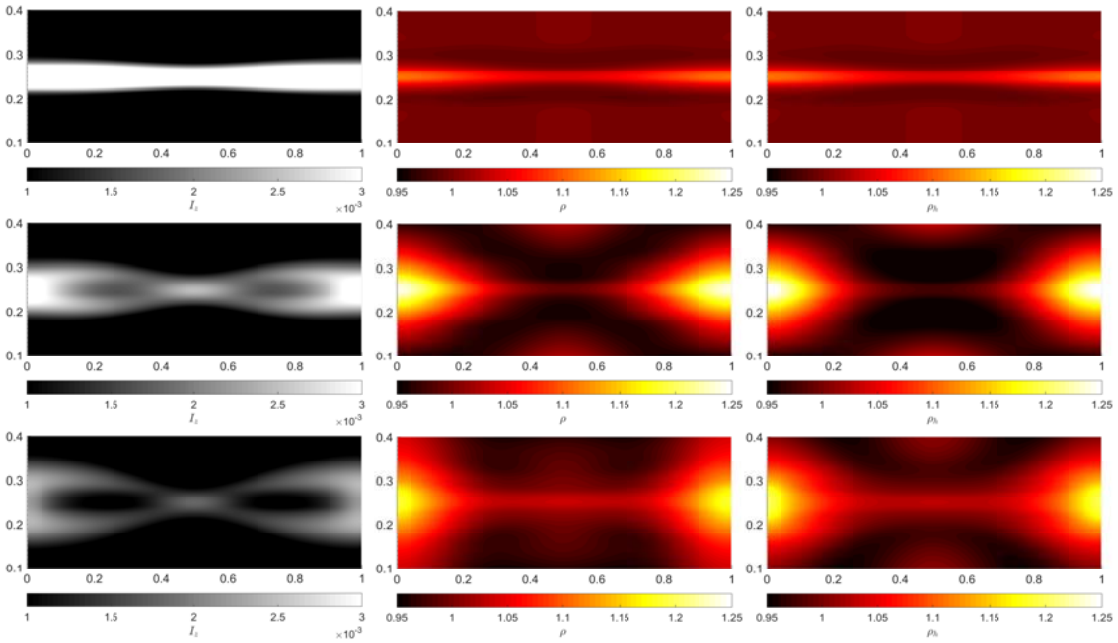

Figure 6: Left and middle: Distribution of the transverse current density and density ρ distribution from the single-fluid MHD model, right: distribution of the total density $\rho = \rho_e + \rho_h$ from the multicomponent model. From top to bottom: $t = 0.05$, 0.1 and $t = 0.4$ respectively.

where the width of the sheet is $\delta/L^* = 0.01$, the amplitude of the perturbation is $\psi_0 = 0.1$, the magnetic field is $B_0 = 1$, the ratio $m_e/m_h = 10^{-3}$, the perturbed magnetic field are

$$B'_x = \psi_0 \pi \cos(2\pi [x - x_c]) \sin(\pi [y - y_c]), \quad \text{and} \quad B'_y = 2\psi_0 \pi \sin(2\pi [x - x_c]) \cos(\pi [y - y_c]).$$

Where $x_c = 1/2$ and $y_c = 1/4$. We choose a $CFL = 0.5$. In order to maintain the divergence free constraint, similarly as in the previous section, we choose $c_h = CFL\,\Delta x/\Delta t$ and $c_p = \sqrt{0.18 c_h}$. The two test cases are run until $t = 0.5$.

Fig. 6 shows the evolution of the transverse current density and the density for the single fluid MHD model (left and middle), and the evolution of the total density for the multicomponent model (right), at time $t = 0.05, 0.1$ and $t = 0.4$. Fig. 7, at the top, shows the distribution of the internal energy of electron at time $t = 0.1$ for the single fluid MHD model and multicomponent model in highly collisional regime. Fig. 7, at the bottom, shows the distribution of the internal energy of electron and the ratio between the internal energy of electron and heavy particle, for the multicomponent model, in the weakly collisional regime, at time $t = 0.1$.

In Fig. 6 and Fig. 7, we clearly see the dynamics of the magnetic reconnection. In Fig. 6, if we focus on the evolution of the transverse current, we see that the magnetic lines are changing their topology forming a current sheet in the center of the domain and two separatrices. The results show that the density is decreasing in the middle of the reconnection but is increasing after the reconnection process. This is due to the mechanism of the magnetic reconnection where the particles are outflowing the reconnection region in the y direction. We retrieve this dynamics of the reconnection, which can be found in the literature involving different initial conditions [2]. Finally, in Fig. 6, if we focus on the evolution of the density and compare the results from the multicomponent and single fluid MHD model (middle and right figures), we see that the dynamics of the reconnection is similar for both models, in the highly collisional regime. Besides, in Fig. 7, at the top, we see that the distribution of the electron internal energy at $t = 0.1$ is similar for the two models (left and right snapshots). In addition, we highlight the

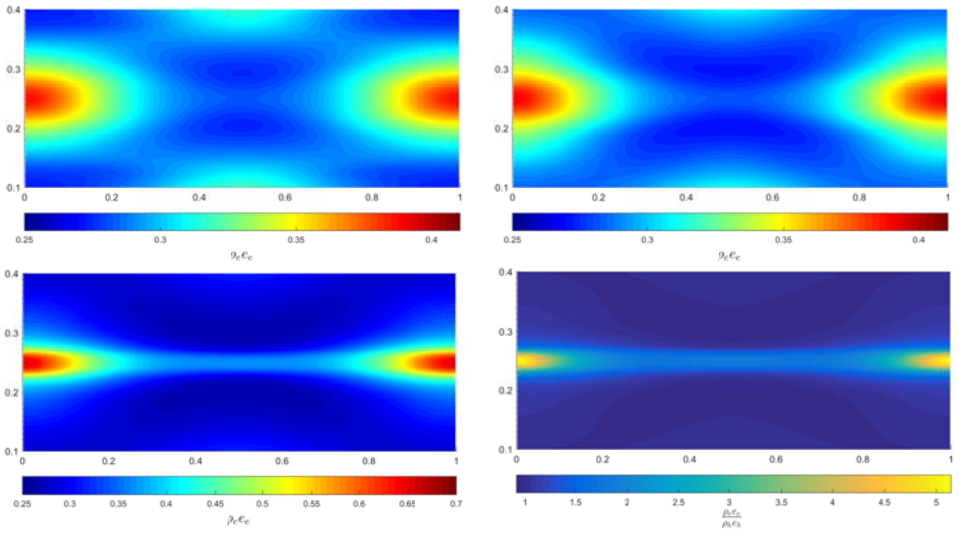

Figure 7: Top: Distribution of the internal energy of electrons for the single fluid-MHD model (left), the multicomponent model (right) in the highly collisional regime, at $t = 0.1$. Bottom: Distribution of the internal energy of electron in the weakly collisional regime (left), distribution of the ratio between internal energy of electrons and heavy particles in the weakly collisional regime (right), at $t = 0.1$.

low additional computing cost required to solve the multicomponent system compared to the resolution of the single-fluid MHD model.

Under the same conditions, we have tested a configuration where the multicomponent model is in a weakly collisional regime. In order to force the system to be in this regime, we take an artificial high mean collision time τ^* such as $\tau^*/t^* \approx 10^3$, which can be representative of a weakly collisional regime. Physically, these regimes can be found in the solar corona. Fig. 7, on the bottom left, represents the distribution of the internal energy of electrons, and Fig. 7, on the right, represents the ratio between the internal energy of electrons and heavy particles, at the time $t = 0.1$. We see that the dynamic of the reconnection is different for the strongly collisional regime. The internal energy of electrons becomes higher in the reconnection region as well as in the magnetic islands. From Fig. 7, we estimate that in the reconnection region $\rho_\mathfrak{e} e_\mathfrak{e} \approx 1.85 \rho_\mathfrak{h} e_\mathfrak{h}$ and in the magnetic islands we have $\rho_\mathfrak{e} e_\mathfrak{e} \approx 5 \rho_\mathfrak{h} e_\mathfrak{h}$. In this configuration, the internal energy distribution between the electrons and heavy particles becomes different, due to the power developped by the electromagnetic field present in the equation of internal energy of electrons. We have an imbalance between the temperature of electrons and the temperature of heavy particles. The impact of the thermal non-equilibrium process on the dynamics transfer is still a work in progress.

5. Conclusion

In this contribution, we have considered a two-temperature single-momentum multicomponent diffusion model as derived by Graille *et al.* [4] and is coupled to Maxwell equations in the small Debye length limit. The model is valid for partially- and fully-ionized plasma, for unmagnetized to weakly- and strongly-magnetized plasmas, and for general multicomponent mixtures. The model is also valid under several collisional regimes (highly or weakly) and is relevant in solar physics applications. It is compared to the multicomponent approach introduced with a classical thermal equilibrium single-fluid MHD model [22]. The single-fluid MHD model is written in a conservative form, and does not represent regimes where there is thermal non-equilibrium thus only valid in highly collisional regimes.

We have also developed a numerical strategy and implemented the two models into a massively parallel code, `CanoP`. It relies on the `p4est` library, which is a parallel scalable implementation of cell-

based adaptive mesh refinement for distributed memory computing systems. The transport properties are computed by another library that is called `MUTATION++`, which has been coupled to the `CanoP` code. In order to verify the implementation of the two models, we have run several classical test cases such as the Orszag-Tang or the rotor MHD problem. The results have shown that the level of accuracy of the presented scheme, the implementation of the convective fluxes and the ability to maintain the divergence free constraint have been verified for both models.

Finally, the two models have been compared in a two dimensional magnetic reconnection configuration under Sun photosphere conditions. The chosen conditions are in a highly collisional regime, where both models are valid. The results have shown that the dynamics of the reconnection are very similar in both models. Thus, the presented multicomponent model has been validated in the highly collisional regime. Then, we have artificially decreased the collisional time in order to mimic a magnetic reconnection configuration in a weakly collisional regime under the same initial conditions. In this configuration, the thermal non-equilibrium between electrons and heavy particles induces a change of dynamics of the magnetic reconnection since the internal energy of electrons is increasing in the reconnection region as well as in the formed magnetic islands, because of the power developed by the electromagnetic field (Joule effect). We believe that these results illustrate the potential of the proposed model and assesses the proposed numerical strategy. We are also in the process of investigating numerical analysis of the numerical method, the parallel scalability of the code and the adaptive mesh refinement capabilities for 3D magnetic reconnections in a subsequent paper [14].

6. Acknowledgments

The research of Q. Wargnier is funded by an Idex Paris Saclay Interdisciplinary (IDI) PhD grant, and relies on the support of *NASA* Ames Research Center (ARC), Advanced Supercomputing Division, von Karman Institute for Fluid Dynamics, CMAP - Initiative HPC@Maths from Ecole Polytechnique and from Ecole doctorale de Mathematiques Hadamard. Part of this work was conducted during the 2018 NASA Summer Program at ARC. A. Alvarez Laguna acknowledges the postdoctoral fellowship from the Fondation Mathematique Jacques Hadamard (FMJH)

References

[1] J. E. Leake, V. S. Lukin, M. G. Linton, and E. T. Meier. Multi-fluid simulations of chromospheric magnetic reconnection in a weakly ionized reacting plasma. *Astrophysical Journal*, 760:109, 2012.

[2] A. Alvarez Laguna, A. Lani, H. Deconinck, N. N. Mansour, and S. Poedts. A fully-implicit finite-volume method for multi-fluid reactive and collisional magnetized plasmas on unstructured meshes. *J. Comput. Phys.*, 318:252–276, 2016.

[3] A. Alvarez Laguna, N. Ozak, A. Lani, N. Mansour, H. Deconinck, and S. Poedts. A versatile numerical method for the multi-fluid plasma model in partially- and fully-ionized plasmas. *Journal of Physics: Conference Series*, 1031:012015, 05 2018.

[4] B. Graille, T. E. Magin, and M. Massot. Kinetic theory of plasmas: translational energy. *Mathematical Models and Methods in Applied Sciences*, 19(04):527–599, 2009.

[5] J. E. Leake, V. S. Lukin, and M. G. Linton. Magnetic reconnection in a weakly ionized plasma. *Physics of Plasmas*, 20(6):061202, June 2013.

[6] E. Khomenko. On the effects of ion-neutral interactions in solar plasmas. *Plasma Physics and Controlled Fusion*, 59(1):014038, January 2017.

[7] E. Khomenko, M. Collados, A. Díaz, and N. Vitas. Fluid description of multi-component solar partially ionized plasma. *Physics of Plasmas*, 21(9):092901, 2014.

[8] L. Ni, V. S. Lukin, N. A. Murphy, and J. Lin. Magnetic reconnection in the low solar chromosphere with a more realistic radiative cooling model. *Physics of Plasmas*, 25(4):042903, April 2018.

[9] F. Drui. *Eulerian modeling and simulations of separated and disperse two-phase flows : development of a unified modeling approach and associated numerical methods for highly parallel computations*. Centralesupélec, Université Paris-Saclay, 2017. https://tel.archives-ouvertes.fr/tel-01618320/en.

[10] M. Essadki, S. de Chaisemartin, M. Massot, F. Laurent, A. Larat, and S. Jay. Adaptive mesh refinement and high order geometrical moment method for the simulation of poly-disperse evaporating sprays. *Oil and Gas Science and Technology*, 71(5):61–86, 2016.

[11] C. Burstedde, L. Wilcox, and O. Ghattas. p4est: Scalable algorithms for parallel adaptive mesh refinement on forests of octrees. *SIAM Journal on Scientific Computing*, 33(3):1103–1133, 2011.

[12] J. B. Scoggins and T. E. Magin. Development of Mutation++: Multicomponent thermodynamic and transport properties for ionized plasmas written in C++. *11th AIAA/ASME Joint Thermophysics and Heat Transfer Conference*, jun 2014.
[13] Q. Wargnier, A. Alvarez-Laguna, J. B. Scoggins, N. N. Mansour, M. Massot, and T. Magin. Consistent transport properties in a two temperature multicomponent plasma model: application to the sun chromosphere. *ArXiv e-prints*, 2018. https://arxiv.org/abs/1810.08490.
[14] Q. Wargnier, A. Alvarez Laguna, T. Magin, M. Massot, B. Graille, and P. Kestener. Mathematical modeling and high performance computing simulation of astrophysical plasmas: application in solar physics. In *NASA Technical Memorandum: Proceedings of the 2018 NASA Summer Program, Nasa Ames Research Center - Advanced Supercomputing Division*, 2018.
[15] R. Balescu. *Transport Processes in Plasmas: Classical transport*. Transport Processes in Plasmas. North-Holland, 1988.
[16] S. I. Braginskii. Transport Processes in a Plasma. *Reviews of Plasma Physics*, 1:205, 1965.
[17] V. Zhdanov. *Transport Processes in Multicomponent Plasma*, volume 44. Taylor & Francis Group, 10 2002.
[18] V.M. Zhdanov and A.A. Stepanenko. Kinetic theory of transport processes in partially ionized reactive plasma, ii: Electron transport properties. *Physica A: Statistical Mechanics and its Applications*, 461(Supplement C):310 – 324, 2016.
[19] V.M. Zhdanov and A.A. Stepanenko. Kinetic theory of transport processes in partially ionized reactive plasma, i: General transport equations. *Physica A: Statistical Mechanics and its Applications*, 446(Supplement C):35 – 53, 2016.
[20] J. B. Scoggins, C. P. Knisely, and T. E. Magin. Crossed contributions to electron and heavy-particle transport fluxes for magnetized plasmas in the continuum regime. *AIP Conference Proceedings*, 1786(1):130002, 2016.
[21] Q. Wargnier, S. Faure, B. Graille, T. Magin, and M. Massot. Numerical treatment of the nonconservative product in a multiscale fluid model for plasmas in thermal nonequilibrium: application to solar physics. *ArXiv e-prints*, 2018. https://arxiv.org/abs/1806.10436.
[22] A. A. Wray, K. Bensassi, I. N. Kitiashvili, N. N. Mansour, and A. G. Kosovichev. Simulations of Stellar Magnetoconvection using the Radiative MHD Code 'StellarBox'. *ArXiv e-prints*, July 2015. https://arxiv.org/abs/1507.07999.
[23] A. Kurganov and E. Tadmor. New high resolution central schemes for non linear conservation laws and convection-diffusion equations. *J. Comput. Phys.*, 160:241–282, 2000.
[24] L. C. Woods. *An Introduction to the Kinetic Theory of Gases and magnetoplasmas.*, volume 286. Cambridge University Press, 1995.
[25] T. Magin and G. Degrez. Transport properties of partially ionized and unmagnetized plasmas. *Phys. Rev. E*, 70:046412, Oct 2004.
[26] M. G. Haines. 'transport processes in plasmas' vol. 1: Classical transport; vol. 2: Neoclassical transport, r. balescu, north-holland press, 1988. *Journal of Plasma Physics*, 43(3):483–485, 1990.
[27] J. Yang and C. Liang. A high-order flux reconstruction adaptive mesh refinement method for magnetohydrodynamics on unstructured grids. *International Journal for Numerical Methods in Fluids*, 86(3):231–253, 2018.
[28] A. K. Fontes Gomes, M. O. Domingues, K. Schneider, O. Mendes, and R. Deiterding. An adaptive multiresolution method for ideal magnetohydrodynamics using divergence cleaning with parabolic–hyperbolic correction. *Applied Numerical Mathematics*, 95:199 – 213, 2015.
[29] G. D. van Albada, B. van Leer, and W. W. Roberts, Jr. A comparative study of computational methods in cosmic gas dynamics. *Astronomy & Astrophysics*, 108:76–84, 1982.
[30] S. Descombes, M. Duarte, T. Dumont, F. Laurent, V. Louvet, and M. Massot. Analysis of operator splitting in the nonasymptotic regime for nonlinear reaction-diffusion equations. Application to the dynamics of premixed flames. *SIAM Journal on Numerical Analysis*, 52(3):1311–1334, 2014.
[31] S. A. Orszag and C-M. Tang. Small-scale structure of two-dimensional magnetohydrodynamic turbulence. *Journal of Fluid Mechanics*, 90(1):129–143, 1979.
[32] D. S. Balsara and D. S Spicer. A staggered mesh algorithm using high order godunov fluxes to ensure solenoidal magnetic fields in magnetohydrodynamic simulations. *J. Comput. Phys.*, 149(2):270 – 292, 1999.
[33] P. Londrillo and L. Del Zanna. High-order upwind schemes for multidimensional magnetohydrodynamics. *The Astrophysical Journal*, 530(1):508, 2000.
[34] A. J. Christlieb, J. A. Rossmanith, and Q. Tang. Finite difference weighted essentially non-oscillatory schemes with constrained transport for ideal magnetohydrodynamics. *J. Comput. Phys.*, 268:302 – 325, 2014.
[35] G. Tóth. The div·B=0 constraint in shock-capturing magnetohydrodynamics codes. *J. Comput. Phys.*, 161(2):605 – 652, 2000.
[36] A. Mignone, C. Zanni, P. Tzeferacos, B. van Straalen, P. Colella, and G. Bodo. The pluto code for adaptive mesh computations in astrophysical fluid dynamics. *The Astrophysical Journal*, 198(1):7, 2012.